Open access • Journal Article • DOI:10.1007/S10494-016-9737-2

Coherent structures in a non-equilibrium large-velocity-defect turbulent boundary layer — Source link

Yvan Maciel, Mark P. Simens, Ayse G. Gungor

Institutions: Laval University, Technical University of Madrid, Istanbul Technical University

Published on: 01 Jan 2017 - Flow Turbulence and Combustion (Springer Netherlands)

Topics: Boundary layer thickness, Boundary layer control, Boundary layer, Blasius boundary layer and Adverse pressure gradient

Flow Turbulence Combust manuscript No.
(will be inserted by the editor)

Coherent structures in a non-equilibrium large-velocity-defect turbulent boundary layer

Yvan Maciel · Mark P. Simens · Ayse G. Gungor

Received: date / Accepted: date

Abstract The characteristics of the coherent structures in a strongly decelerated large-velocity-defect boundary layer are analysed by direct numerical simulation. The simulated boundary layer starts as a zero-pressure-gradient boundary layer, decelerates under a strong adverse pressure gradient, and separates near the end of the domain, in the form of a very thin separation bubble. The Reynolds number at separation is $Re_\theta = 3912$ and the shape factor $H = 3.43$. The three-dimensional spatial correlations of (u, u) and (u, v) are investigated and compared to those of a zero-pressure-gradient boundary layer and another strongly decelerated boundary layer. These velocity pairs lose coherence in the streamwise and spanwise directions as the velocity defect increases. In the outer region, the shape of the correlations suggest that large-scale u structures are less streamwise elongated and more inclined with respect to the wall in large-defect boundary layers. The three-dimensional properties of sweeps and ejections are characterized for the first time in both the zero-pressure-gradient and adverse-pressure-gradient boundary layers, following the method of Lozano-Durán et al. (J. Fluid Mech., vol. 694, 2012). Although longer sweeps and ejections are found in the zero-pressure-gradient boundary layer, with ejections reaching streamwise lengths of 5 boundary layer thicknesses, the sweeps and ejections tend to be bigger in the adverse-pressure-gradient boundary layer. Moreover, small near-wall sweeps and ejections are much less numerous in the large-defect boundary layer. Large sweeps and ejections that reach the wall region (wall-attached) are also less numerous, less streamwise elongated and they occupy less space than in the zero-pressure-gradient boundary layer.

Y. Maciel
Department of Mechanical Engineering, Laval University, Quebec City, QC, G1V 0A6 Canada
E-mail: yvan.maciel@gmc.ulaval.ca

M. P. Simens
School of Aeronautics, Universidad Politécnica de Madrid, 28040 Madrid, Spain
E-mail: markphilsimens@gmail.com

A. G. Gungor
Faculty of Aeronautics and Astronautics, Istanbul Technical University, 34469 Maslak, Istanbul, Turkey
E-mail: ayse.gungor@itu.edu.tr

Keywords Turbulence simulation · Turbulent boundary layers · Wall-bounded turbulence · Adverse pressure gradient · coherent structures · two-point correlations · quadrant analysis

1 Introduction

A turbulent boundary layer (TBL) subjected to a strong or prolonged adverse pressure gradient (APG) develops a large mean velocity defect. The mean shear rates in the outer region are no longer small in comparison to their near-wall counterparts while near the wall, the importance of viscous forces and of the wall shear stress diminishes. As a result, in contrast to canonical wall-bounded turbulent flows, turbulence activity and production is small near the wall and important in the outer region of the flow [27,18,3]. Marquillie et al. [15] have proposed that the outer peaks of Reynolds stresses and production could be related to a streak bursting process, whereas Elsberry et al. [3] suggest that it is due to the inflectional instability of the mean velocity profile as in mixing layers. By analysing three different large-velocity-defect TBLs and by assuming the local mean shear to be the source of turbulent energy, Gungor et al. [4,5] have concluded that these boundary layers are globally less efficient in extracting turbulent energy from the mean flow than the zero-pressure gradient (ZPG) TBL. The Reynolds stresses and the production of turbulent kinetic energy were found to be weaker in the lower half of the large-velocity-defect boundary layers than in the ZPG TBL. Furthermore, the outer-region turbulent statistics of TBLs close to detachment were found to resemble those of single-stream mixing layers. These various observations suggest that the physical mechanisms and coherent structures responsible for the production and transport of turbulence might indeed be different in APG TBLs.

Coherent motions have been identified and analyzed in the different regions of canonical wall-bounded turbulent flows extensively. Recent reviews with different viewpoints can be found in Refs. [17],[10] and [9]. In the near-wall region, a self-sustaining regeneration process involving streaky u structures and quasi-streamwise vortices is generally accepted, albeit conceptual scenarios vary. The consensus is less clear regarding the coherent structures and dynamical processes found in the logarithmic and wake outer regions of these flows. By interpreting spatial correlations of the streamwise velocity fluctuations, Townsend [28] inferred one of the first physical pictures of the large-scale motions in turbulent wall-bounded flows, namely the hypothesis of an hierarchy of self-similar attached (extending to the wall) energy-containing motions. This hypothesis is at the base of the two dominant and opposing paradigms about the coherent structures found in the logarithmic and wake outer regions. One of these paradigms [17] considers groups of streamwise organized hairpin vortices, termed hairpin packets [1], as being the building block. These packets of vortices are assumed to originate close to the wall and to grow self-similarly and interact in the spanwise direction. They induce large regions of streamwise momentum deficit. In the second paradigm [9], the streamwise velocity is organized in streaks as in the buffer layer, although much larger ones, but individual vortices lose their role regarding the generation of Reynolds shear stresses due to the smallness of their scale and their more disorganized (or isotropic) character. This role is interpreted as being taken over instead by larger structures: vortex clusters and large-scale ejections and sweeps, whose

spatial organization is compatible with the inferred presence of streamwise large-scale rollers that are not directly observable. A temporally intermittent bursting process would be involved in the production of turbulence. In a variation on the same theme, some researchers consider the main mechanism to be the amplification of the long streaky motions by a lift-up effect due, possibly, to packets of vortices (see Hwang [8] for a review of these ideas).

The present study focuses on the u and uv structures because of their recognized role in the dynamic process of turbulence regeneration. Quadrant analysis in the plane of streamwise and wall-normal velocity fluctuations (u, v) has been used extensively in the past to investigate the bursting process close to the wall of canonical wall flows [22] since coherent and intense Q2 (ejection) and Q4 (sweep) events carry most of the Reynolds shear stress and as such they play a crucial role in terms of momentum flux and production of turbulent energy. Quadrant analysis was also used later to study the outer ejection and sweep structures [29]. Lozano-Durán et al. [13] have recently extended the quadrant analysis to three-dimensional structures in a direct numerical simulation (DNS) study of turbulent channel flows. They called Qs the quadrant-splitted three-dimensional uv structures. They found that wall-detached Qs (in the sense of not reaching the wall at their base) are generally background fluctuations while wall-attached Qs are bigger and carry most of the Reynolds shear stress in channel flows. More recently, Lozano-Durán and Jiménez [14] studied the time evolution of these Qs. They found that wall-attached Q2s and Q4s are essentially mirror images of each other and they suggested that they are both manifestations of a single quasi-streamwise roller lying between them. They also showed that their dynamics is controlled by the local mean shear and that most of them are not born close to the wall.

Unfortunately, information on the coherent structures found in APG TBLs is rare. By analyzing the DNS data of a turbulent separation bubble [18], Chong et al. [2] suggested that in the APG zone prior to detachment more of the eddies which contribute to the Reynolds shear stress are eddies which are not connected to the wall. In the case of a large-defect equilibrium APG TBL, Krogstad and Skåre [11] found that the lower part of the boundary layer is strongly dominated by Q4 motions, while in a ZPG TBL second and fourth quadrant events are equally important. The streamwise correlation length of u was also found to be considerably shorter in the APG case throughout the boundary layer, a result also obtained later in non-equilibrium large-velocity-defect TBLs by Rahgozar and Maciel [21] and Gungor et al. [4]. Lee and Sung [12] investigated the APG effect on turbulent structures with DNSs of two equilibrium mild-APG turbulent boundary layers together with a ZPG case. The near-wall streaks became weaker and more irregular as the velocity defect increased. In the APG TBLs, in comparison to the ZPG TBL, the low-speed streaks were found to be shorter throughout the outer region, and more present in the middle of the boundary layer. Harun et al. [6] showed that the large-scale u-structures are more energized by the pressure gradient in the outer region than the small-scale ones in an experimental study of a TBL with a moderate adverse pressure gradient. In a turbulent boundary layer subjected to a strong adverse pressure gradient that eventually separates, Shafiei Mayam [23] found packets of spanwise vortices that have characteristics globally comparable to those found in ZPG TBLs, but these packets were more compact in the streamwise direction and more inclined with respect to the wall. By analyzing the same flow, Rahgozar and Maciel [20] observed that the predominance of large-scale streaky

u-structures in the outer region is less than in the ZPG case. This predominance even disappears near separation. In a subsequent study, Rahgozar and Maciel [21] found that large-scale u-structures are less elongated than those of ZPG TBLs, especially in the lower part of the boundary layer.

In the present work, we investigate how a strong adverse pressure gradient affects the u and uv structures in the case of a non-equilibrium large-velocity-defect TBL. The goal is to advance our knowledge and understanding of APG boundary layer flows. To achieve this goal, we analyze the three-dimensional spatial correlations of (u, u) and (u, v) and the geometric and kinematic characteristics of Q structures, and compare them with those found in a ZPG TBL and another non-equilibrium large-velocity-defect TBL. The present study also provides for the first time information on the three-dimensional properties of Q structures found in ZPG TBLs.

2 Numerical Methodology

The two direct numerical simulations used in this paper have been performed with the same code. The ZPG TBL was simulated by Sillero et al. [24] while the APG TBL simulation is a new one carried out by the present authors. The DNS numerical scheme is described in detail in [26] and [24]. Both flows are simulated in a parallelepiped domain over a smooth no-slip wall, with spanwise periodicity and streamwise non-periodic inflow and outflow. The Navier-Stokes equations are integrated using a fractional step method on a staggered grid, with third-order Runge-Kutta time-integration, fourth order compact spatial discretization for the convective and viscous terms, and second order discretization for the pressure in the directions perpendicular to the span, which is spectral.

The DNS database of the ZPG TBL covers the Reynolds number range $Re_\theta = 2780 - 6680$. As described in Ref. [24], the one-point statistics of the ZPG TBL are in very good agreement with experimental and numerical data. The spatial resolution in viscous-friction units at the middle of the computational box is $\Delta x^+ = 6.5$ and $\Delta z^+ = 3.8$. At that location, the wall-normal resolution varies from $\Delta y^+ = 0.32$ at the wall to 10.2 at $y = \delta$. For both TBLs, δ is the boundary layer thickness defined as the wall-normal position where $U = 0.99U_e(x)$; U is the streamwise component of mean velocity and U_e is the external (freestream) velocity at the edge of the boundary layer which, in the case of the APG flow, is the wall-normal maximum of U.

The DNS computational setup for the present APG TBL simulation is sketched in figure 1. It consists of two simulations running concurrently [24]. The first auxiliary simulation is that of a ZPG TBL and it is intended to provide a realistic turbulent inflow for the APG layer. As in Ref. [24], the inflow of the auxiliary DNS is obtained by rescaling the velocity fluctuations of a downstream plane, while fixing the inflow mean velocity to the DNS profile of Ref. [26] at $Re_\theta = 617$. The recycling plane is located at $x \approx 398\theta_{0,aux} \approx 45\delta_{0,aux}$, where $\theta_{0,aux}$ and $\delta_{0,aux}$ are respectively the momentum and boundary layer thicknesses at the beginning of the auxiliary ZPG DNS. A plane located at $x \approx 268\theta_{0,aux} \approx 30\delta_{0,aux}$ of the first domain is transferred at each time step into the inlet of the second main domain. The velocities at the outflow of the two computational boxes are estimated by a convective boundary condition, where the convection speed is the local velocity. The outflow

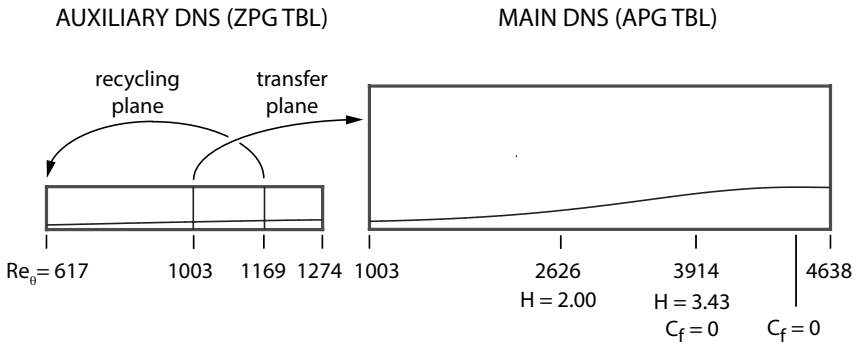

Fig. 1 Schematic in the xy plane of the numerical simulation setup showing the boundary layer thickness

streamwise velocities are corrected to compensate the minimal mass flux variations due to the time-dependent inflows [26]. Table 1 summarizes the simulation parameters for both layers. For the APG DNS, the box dimensions with respect to the boundary layer thickness at the outlet are $(L_x, L_y, L_z)/\delta_{exit} = (11.0, 3.4, 2.6)$. The resolutions in terms of the Kolmogorov length η are $(\Delta x_g, \Delta y_g, \Delta z_g) < 4\eta$ except near the inlet very close to the wall where $\Delta x_g < 8\eta$. After an initial transient phase, statistics and flow fields were sampled over 53,600 time steps corresponding to a total time of $5250\theta_0/U_0$ or 10 flow-through times with respect to U_0, where θ_0 and U_0 are respectively the momentum thickness and freestream velocity at the inlet of the main DNS. A total of 134 instantaneous fields were kept, with a time interval between fields of $39.2\theta_0/U_0$.

3 Flow Description

For the DNS of the APG TBL, the desired pressure gradient is controlled by imposing a streamwise dependent wall-normal velocity distribution at the upper boundary of the computational domain. The wall-normal velocity distribution was chosen to lead to a steady, almost linear increase of the shape factor H in a large portion of the domain. It was obtained numerically with inverse boundary layer computations. The streamwise and spanwise velocities along the top boundary satisfy free-slip conditions. The imposed wall-normal velocity at the top boundary $V(x)/U_0$ and the resulting streamwise velocity at the same boundary $U(x)/U_0$ are illustrated in black in Figs. 2(a) and (b) respectively. The streamwise evolutions of U_e and of the wall-friction velocity $u_\tau = (\tau_w/\rho)^{1/2}$ are also depicted in Fig. 2(b).

Table 1 Parameters of the APG TBL simulation. L_x, L_y, and L_z are the box dimensions along the three axes. N_x, N_y, and N_z are the collocation grid sizes. The momentum thickness θ is measured at the middle of each box.

Case	Re_θ	$(L_x, L_y, L_z)/\theta$	N_x, N_y, N_z
Auxiliary DNS (ZPG TBL)	617-1274	$320 \times 49 \times 126$	$1201 \times 191 \times 768$
Main DNS (APG TBL)	1003-4638	$118 \times 37 \times 28$	$1921 \times 380 \times 768$

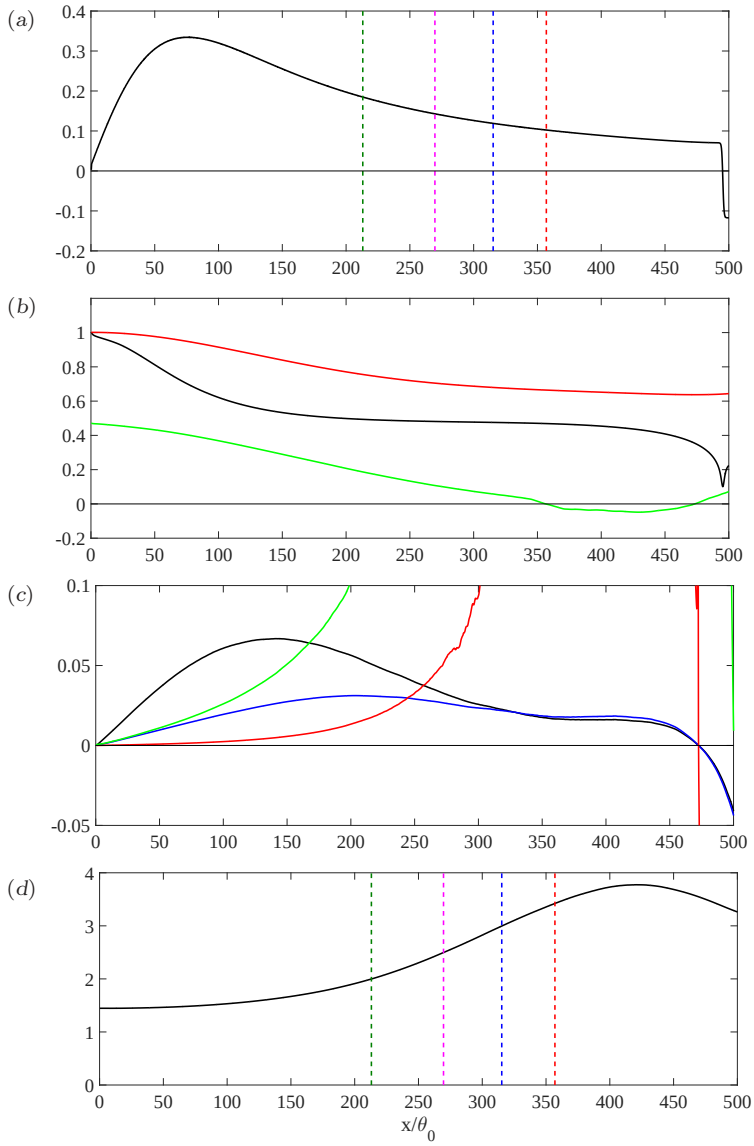

Fig. 2 Mean flow parameters in the APG DNS. (a) Imposed wall-normal velocity along the top boundary. (b) black, Streamwise velocity at the top boundary, ; red, U_e/U_0; green, $10u_\tau/U_0$. (c) Pressure gradient parameters: black, β_m; blue, β_{zs}; red, $\beta_\tau \times 10^{-3}$; green, β_i. (d) Shape factor H. Vertical dashed lines in (a) and (d) denote the four streamwise positions where $H = 2$ (green), 2.5 (magenta), 3 (blue), and 3.43 (red)

From the streamwise evolution of U_e (red curve), it is seen that the flow at the edge of the boundary layer decelerates over most of the domain but then reaccelerates slightly at the end. As can be deduced from the evolution of u_τ (green curve), the wall shear stress decreases and eventually becomes negative. The flow separates near the exit of the domain in the form of a very thin separation bubble. The height of the zone of negative mean streamwise velocity never exceeds 0.02δ. The reacceleration of the flow at the end reattaches the boundary layer and thereby avoids encountering problems with the outflow boundary condition.

Figure 2(c) shows the streamwise evolution of three different outer pressure gradient parameters β_m, β_{zs} and β_τ, as well as the inner pressure gradient parameter $\beta_i = \nu/(\rho u_\tau^3)(dp/dx)$, often denoted p^+ in the literature. The traditional outer pressure gradient parameter, Rotta-Clauser's $\beta_\tau = -(\Delta/u_\tau)(dU_e/dx)$, where $\Delta = \delta^* U_e/u_\tau$, assumes the outer region velocity scale to be u_τ, which is not the case for large-velocity defect TBLs such as the one considered here. β_{zs} and β_m are more appropriate outer pressure gradient parameters since they are based on velocity scales that are valid for both small and large defect TBLs. $\beta_m = -(\delta/U_m)(dU_e/dx)$ is expressed with the mixing-layer-type outer-velocity scale $U_m = 2(U_e - U(y = 0.5\delta))$ introduced by Gungor et al. [4,5]. $\beta_{zs} = -(\delta/U_{zs})(dU_e/dx)$ is based on the Zagarola-Smits velocity scale $U_{zs} = U_e\delta^*/\delta$. Both U_m and U_{zs} are proportional to the mean streamwise momentum deficit in the boundary layer. β_{zs} and β_m are not equivalent but their streamwise evolutions are qualitatively similar, as can be seen in Fig. 2(c).

Figure 2(c) shows that each pressure gradient parameter increases significantly in a different upstream portion of the flow. The positive gradient of these pressure gradient parameters is responsible for the increase in the streamwise mean momentum defect as shown in Fig. 2(d) with the increase of the shape factor H. β_i and β_τ tend to infinity at separation and reattachment since $u_\tau = 0$ there. The outer pressure gradient parameters β_m and β_{zs} start decreasing in the first half of the domain. The impact of the pressure force on the outer region is therefore diminishing but this change is not strong enough to reverse the situation in terms of mean momentum defect, which keeps increasing until flow separation. At separation, $H = 3.43$.

To give a better idea of the streamwise evolution of the APG TBL, selected one-point velocity statistics are presented in Fig. 3. Note that the one-point velocity statistics of this flow have been studied in detail by Gungor et al. [5] who also compared them with those of other large-defect TBLs. In Fig. 3, they are compared to those of the ZPG TBL of Ref. [24] at $Re_\theta = 4000$. For the APG TBL, the four selected streamwise positions correspond to $H = 2, 2.5, 3$ and 3.43. The fourth one is the last mesh position before separation ($C_f \approx 10^{-6}$). The streamwise mean velocity profiles in Fig. 3(a) reveal the progressive increase of the mean velocity defect in the APG TBL. As a result, the mean shear rates increase in the outer region. The velocity defect profiles normalized with U_m are presented in Fig. 3(b). The defect profiles are not identical, as expected from the disequilibrium nature of the flow, but they are all regrouped in the outer region. U_m and δ are therefore appropriate outer scales to compare velocity statistics at various positions of the APG TBL, as well as between ZPG and APG TBLs.

Figure 3(c) shows the profiles of the Reynolds shear stress normalized with U_m. In the present APG TBL, the maximum of the Reynolds shear stress moves away from the wall as the velocity defect increases, reaching the middle of the

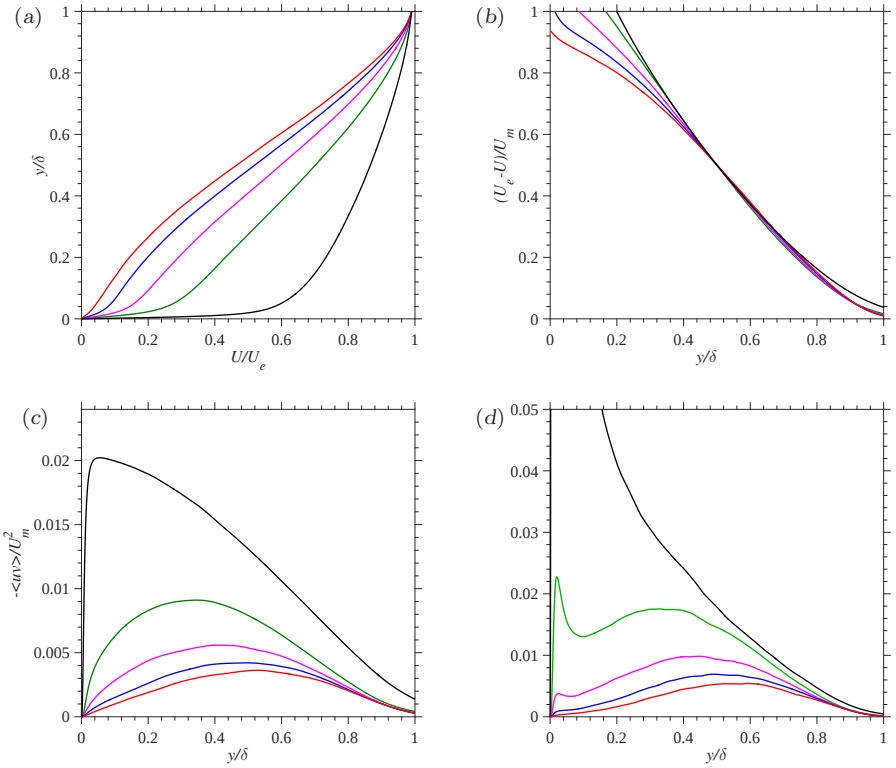

Fig. 3 Velocity statistics normalized by U_m and δ: (a) Mean velocity, (b) Mean velocity defect, (c) Reynolds shear stress, (d) Production of turbulent kinetic energy. APG TBL: green, $H = 2.0$; magenta, $H = 2.5$; blue, $H = 3.0$; red, $H = 3.43, C_f = 0$. Black, ZPG TBL of Ref. [24] at $Re_\theta = 4000$

boundary layer near separation. In relation to the outer velocity scale U_m, the Reynolds shear stress decreases at all wall-normal positions but more importantly so in the lower half of the boundary layer. Gungor et al. [4,5] have shown that these characteristics are common to all Reynolds stresses for three different types of large-defect TBLs. The difference between ZPG and large-defect APG TBLs is even more pronounced for the production of turbulent kinetic energy shown in Fig. 3(d) normalized with U_m and δ. As the velocity defect increases, the near-wall production peak decreases very rapidly and vanishes near separation. A production maximum appears in the outer region and its shift away from the wall follows that of the maximum of the Reynolds stresses. Since U_m is proportional to the mean shear rates present in the outer region, Fig. 3(d) indicates that the present large-defect TBL is globally less efficient in extracting turbulent energy from the mean flow than the ZPG one. Gungor et al. [4,5] have also shown that for two other types of large-defect TBLs.

4 Results

4.1 Visualization of instantaneous structures

In order to illustrate global features of the coherent structures, isosurfaces of instantaneous u and uv are visualized and analyzed. These variables are normalized by their respective local standard deviations to avoid introducing a streamwise and wall-normal bias due to their spatially varying magnitudes. Normalization by the standard deviation scales the fluctuating variable with its local characteristic magnitude at the given location. It is consistent with quadrant analysis, with the definition of the Q structures in Sect. 4.3, as well as with many studies on coherent structure identification and characterization since Nagaosa and Handler [19].

Figure 4 shows different views of instantaneous isosurfaces of $u/\sigma_u = -1.75$ (red) and $u/\sigma_u = +1.75$ (blue), where $\sigma_u(x, y)$ is the local standard deviation of u, in a subvolume of cross-section $0.3L_y \times 0.5L_z$. The isovalue 1.75 gives a good compromise between visualizing only a few small intense u structures and voluminous structures that all become connected. The rapid spatial growth of the structures can be appreciated with the perspective and top views of low-speed structures in Figs. 4(a) and (b) respectively. The large-scale outer u structures, both low and high speed ones, are often streamwise elongated, inclined with respect to the wall and streamwise aligned. They resemble in that respect the long streaky u structures found in the logarithmic region of ZPG TBLs [7].

The side views of Fig. 4(c) suggest that high-speed structures tend to be closer to the wall than low-speed structures. Such a trend has also been observed in two experimental studies of large-defect APG TBLs. For instance, in a non-equilibrium APG TBL, Rahgozar and Maciel [20] found that strong low-speed motions appear more frequently above $y \approx 0.4\delta$, whereas high-speed ones are predominant below. Although they did not study u-structures, Krogstad and Skåre [11] showed that, contrary to a ZPG TBL, a large-defect equilibrium TBL is totally dominated by strong Q1 and Q4 motions near the wall, hence positive u events although they are not necessarily all strong ones. Q2 motions were found to be predominant above $y \approx 0.4\delta$. It will be seen below that the wall-normal distribution of Q2 and Q4 motions is similar in the present flow.

In Fig. 4(c) one can also note that when the mean velocity defect becomes large, $H > 2$, u structures appear less frequently near the wall. The near-wall behaviour of the u structures can however be better appreciated with the top view of Fig. 5. In this figure, only the isosurfaces of u in the layer between the wall and $y = 0.05\delta$ are shown. The boundary layer thickness δ is used as the length scale since we do not know of an inner length scale valid everywhere for a non-equilibrium flow with large streamwise variations. The two dashed squares are visual aids proportional to δ, that is to the growth of the boundary layer. They allow a comparison of the shape, size and density of the u structures in small-velocity-defect and large-velocity-defect regions of the flow. The near-wall u structures are found to become less and less streaky as the velocity defect increases. The destruction of the near-wall streaks just upstream of and in the separation region of separated boundary layer flows has also been observed by Na and Moin [18] and Marquillie et al [16]. By comparing the u structures inside the two white dashed squares, one can see that they occupy less space in the large-defect case. Spanwise elongated structures

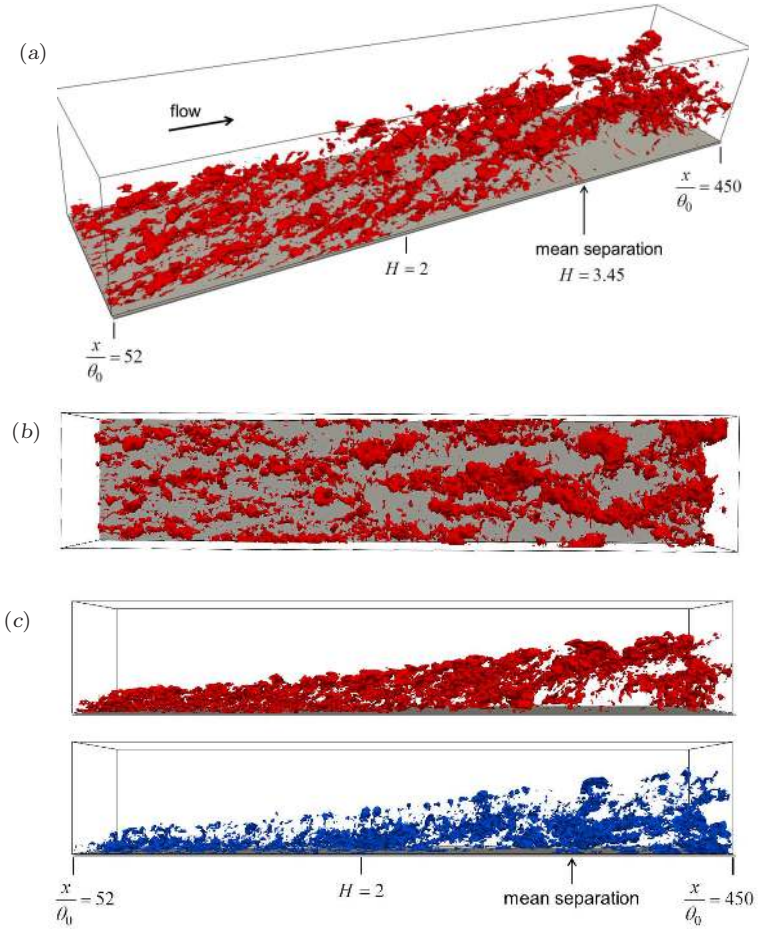

Fig. 4 Instantaneous isosurfaces of $u = -1.75\sigma_u$ (red) and $u = +1.75\sigma_u$ (blue) in a subvolume of cross-section $0.3L_y \times 0.5L_z$. Perspective (a) and top (b) views of low-speed u. (c) Side views of low- and high-speed u

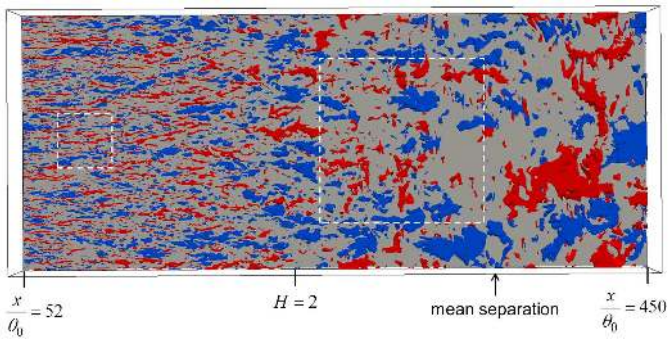

Fig. 5 Top view of the instantaneous isosurfaces of $u = -1.75\sigma_u$ (red) and $u = +1.75\sigma_u$ (blue) in the layer between the wall and $y = 0.05\delta$. Dashed squares have a linear dimension of about $2.6\delta_a$ where δ_a is the average δ over the square

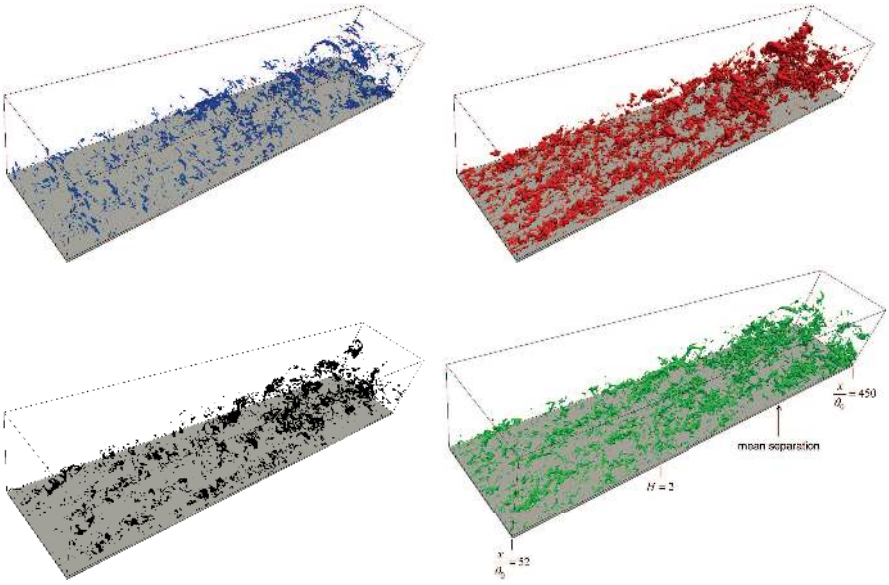

Fig. 6 Instantaneous isosurfaces of $(uv)_{Q_1} = 1.75\sigma_u\sigma_v$ (blue), $(uv)_{Q_2} = -1.75\sigma_u\sigma_v$ (red), $(uv)_{Q_3} = 1.75\sigma_u\sigma_v$ (black), and $(uv)_{Q_4} = -1.75\sigma_u\sigma_v$ (green) for the same field and subvolume as in Fig. 4

also start appearing in the zone where instantaneous reverse flow occurs near the wall.

Figure 6 shows instantaneous isosurfaces of $uv/(\sigma_u\sigma_v)$ split according to the quadrant in the (u, v) plane, for the same field and subvolume as in Fig. 4. The same isovalue of 1.75 is used for all quadrants. It is identical to the threshold value selected via the percolation method in Sect. 4.3 to extract the Q structures. The instantaneous objects shown in this figure are therefore the Q structures of Sect. 4.3. The positive uv structures (Q1 and Q3) are smaller than the negative ones (Q2 and Q4). The latter tend to be streamwise elongated and the longest structures appear to be Q2 structures. These features are confirmed by the statistical analysis of Sect. 4.3. The Q2 and Q4 regions shown in Fig. 6 are often almost coincident with, respectively, the low-speed and high-speed regions of Fig. 4, but they are smaller and less streamwise elongated.

4.2 Two-point correlations

The spatial organization of u and uv is now investigated using three-dimensional spatial correlations. In physical space, the two-point cross-correlation coefficient for two generic variables a and b is defined as

$$C_{ab}(\mathbf{r}, \mathbf{r'}) = \frac{\langle a(\mathbf{r})b(\mathbf{r'})\rangle}{\sigma_a(\mathbf{r})\sigma_b(\mathbf{r'})}, \tag{1}$$

where $\mathbf{r}$ is the reference position and $\mathbf{r'}$ the moving one. The averaging is over time and spanwise direction. The correlation functions are actually computed in Fourier space in the homogeneous spanwise direction and then Fourier transformed.

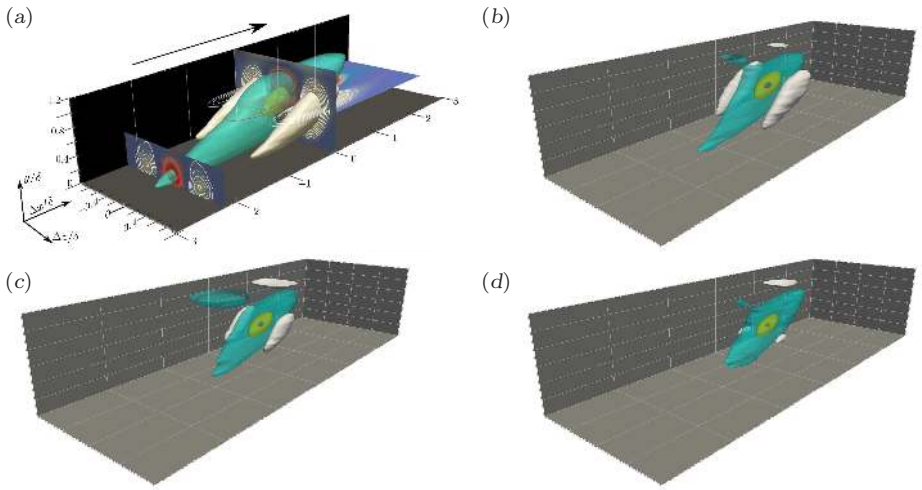

Fig. 7 Three-dimensional views of C_{uu} with reference point at $y = 0.6\delta$. (a) ZPG TBL of Ref. [24] at $Re_\theta = 4850$ (Fig. 1 of [25] with permission from AIP). APG TBL at positions corresponding to (b) $H = 2$ (c) $H = 2.5$ and (d) $H = 3.45$. Isosurfaces at $C_{uu} = -0.09$ (white), $+0.09$ (turquoise), $+0.4$ (yellow) and $+0.8$ (blue). Same axes ranges in all four plots

Figure 7 presents three-dimensional views of C_{uu} with the reference point at $y = 0.6\delta$ for three streamwise positions of the APG TBL corresponding to $H = 2$, 2.5 and 3.45 (separation). The three-dimensional representation of Sillero et al. [25] for their ZPG TBL at $Re_\theta = 4850$ is also included in the figure for comparison. The four plots are for a domain of size $6\delta \times 1.2\delta \times 2\delta$ in x, y and z respectively, centered at the reference point. The isosurfaces $C_{uu} = 0.09$ (turquoise) and $C_{uu} = -0.09$ (white) clearly show that the regions of positive and negative coherence of u are shorter and more inclined with respect to the wall for the large-defect TBL in comparison to a ZPG TBL. It suggests that large-scale u structures are shorter and more inclined in this large-defect TBL. The streamwise extent of the isosurface $C_{uu} = 0.09$ is about 4δ for the ZPG TBL and 2δ for the APG TBL. Moreover, both the positive and negative regions become smaller as the velocity defect increases. The negative-positive-negative spanwise trend loses coherency.

Figure 8 presents streamwise-spanwise sections of C_{uu} at $y = 0.2\delta$ (bottom row) and $y = 0.5\delta$ (top row). These wall-normal reference positions allow a comparison with the two-dimensional C_{uu} results of Rahgozar and Maciel [21] for a different large-defect APG TBL that also separates. The same contour levels are used in all the maps of this figure. The contours at low correlation values of the present APG TBL at separation are not statistically converged (noisy) because of the large u fluctuations at that position caused by the unsteady character of the separation bubble. They are therefore not considered in the analysis. More statistically independent realizations would have been necessary to obtain converged results. At the two heights, the streamwise extent of the positive C_{uu} contours in both large-defect TBLs is shorter than in the ZPG TBL. The difference is however smaller for the APG TBL of Rahgozar and Maciel. Similar trends were observed in equilibrium APG TBLs by Krogstad and Skåre [11] in a large-defect case ($H = 2$)

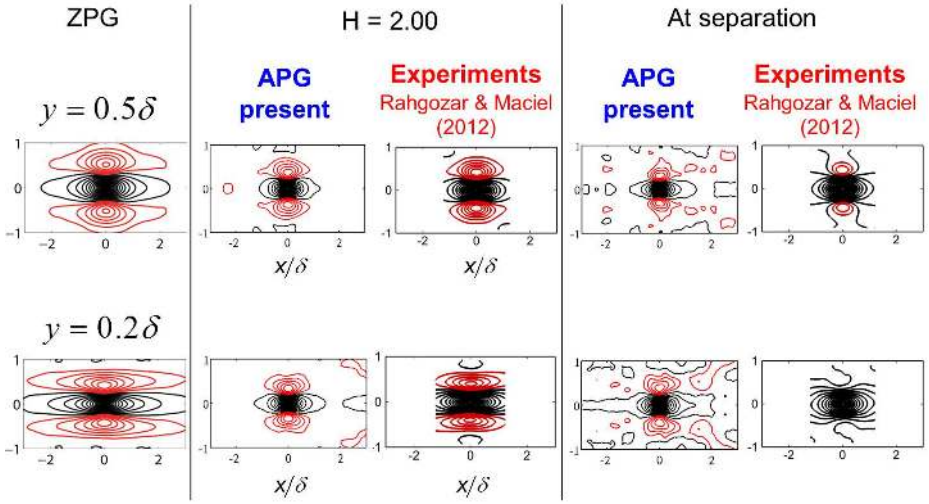

Fig. 8 Streamwise-spanwise maps of C_{uu} for three different flows: ZPG TBL of Sillero et al. [25] at $Re_\theta = 4850$, large-defect APG TBL of Rahgozar and Maciel [21] at $H = 2$ and at separation, and present APG TBL at $H = 2$ and at separation. Reference point at $y = 0.2\delta$ (bottom row) and $y = 0.5\delta$ (top row). Positive contours (black) start at 0.02 by increments of 0.05. Negative contours (red) start at -0.02 by increments of -0.03

and by Lee and Sung [12] in a small-defect case (mild APG). The spanwise extent of the positive contours is slightly smaller in the present APG flow compared to the two other flows shown in the figure.

In both APG TBLs, the negative C_{uu} contours are much smaller than in the ZPG TBL and they shrink in size as the velocity defect increases. In the case of the APG TBL of Rahgozar and Maciel, they have disappeared at separation at $y = 0.2\delta$ and negative coherence is very weak at $y = 0.5\delta$. These results suggest that the alternating-sign streaky pattern of large-scale u structures occurs less frequently as the defect increases.

Streamwise-wall-normal maps of C_{vu} are shown in Fig. 9 for a reference point at $y = 0.4\delta$. At that wall-normal height, the Reynolds shear stress is high in the APG TBL as shown in Fig. 3(c). For the APG TBL, the low-level contours are noisy due to the insufficient number of statistically independent flow realizations. As expected, the negative value of the cross-correlation indicates that Q2 and Q4 motions are dominant. It is interesting to note that for all the cases shown in Fig. 9 there is a different behaviour between the high negative level contours close to the reference point and the low negative level contours further away. The contours near the reference point are compact and inclined in the upstream direction by about 135°. They reflect the character of smaller-scale intense Q2 and Q4 motions and the inclination angle is similar to what Adrian et al. [1] have observed for strong Q2 and Q4 motions in a ZPG TBL. This inclination angle is maintained as the velocity defect increases. The weak larger-scale contours are streamwise elongated in the case of the ZPG TBL and inclined in the downstream direction. They resemble the C_{uu} contours in the same plane (not shown). Sillero et al. [25] suggested that they probably reflect the combination of long u streaks with a smaller sweep or ejection motion. In the case of the APG TBL, the streamwise elongation of the

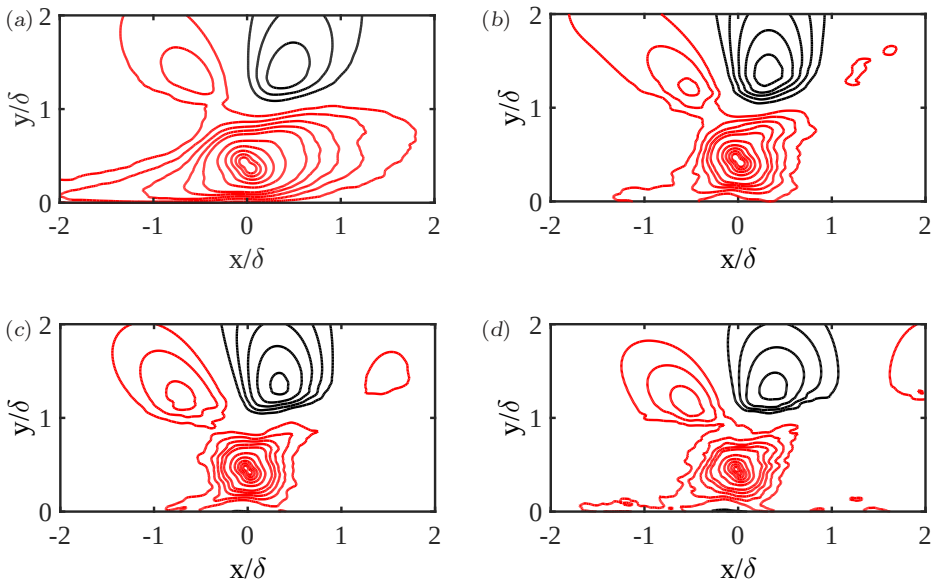

Fig. 9 Streamwise-wall-normal maps of C_{vu} with reference point at $y = 0.4\delta$. (a) ZPG TBL of Ref. [24] at $Re_\theta = 4850$. APG TBL at positions corresponding to (b) $H = 2$ (c) $H = 2.5$ and (d) $H = 3.45$. Positive contours (black) start at 0.03 by increments of 0.02. Negative contours (red) from -0.03 to -0.11 by increments of -0.02, from -0.16 to -0.36 by increments of -0.05

weak large-scale contours is reduced and the inclination with respect to the wall is increased. The large-scale C_{uu} contours exhibit similar trends (not shown).

4.3 Q structures

Although they provide valuable statistical information on the structure of turbulence, two-point correlations mix the signatures of various types of coherent structures of a wide spectrum of sizes. For this reason, we now extract and directly analyze the intense three-dimensional uv structures (Qs) in both the ZPG TBL of Sillero et al. [24] and in the present APG TBL. The procedure adopted to identify the Qs follows the method used by Lozano-Durán et al. [13] (hereafter denoted LFJ). The Qs are defined as regions of connected points that satisfy simultaneously two conditions. The first condition is $|u(\mathbf{r})v(\mathbf{r})| > H^*\sigma_u\sigma_v$, where H^* is the threshold constant discussed below, also called hyperbolic-hole size. LFJ give a detailed justification of the choice of $H^*\sigma_u\sigma_v$ as the threshold function. The second condition is that all points within a Q structure are in the same quadrant of the u, v space. Point connectivity is defined with the six orthogonal neighbours. Following the notation of LFJ, the Q2 and Q4 structures will be referred to as Q^-s, and the Q1s and Q3s as Q^+s.

Table 2 presents the parameters of the subdomains used for the extraction of the Q structures. For the APG TBL, the extraction box covers the zone of large velocity defect of the flow prior to separation. The streamwise extent of

the box is $5\delta_a$ where δ_a is the average boundary layer thickness inside the box. The streamwise position of the box for the ZPG TBL gives ranges of the three Reynolds numbers comparable to those of the APG TBL. $Re_m = U_m\delta/\nu$ and $Re_{zs} = U_{zs}\delta/\nu$ are Reynolds numbers of the outer region. Both extraction boxes cover the full width of the simulation domain. The same wall-normal height of $2\delta_a$ was chosen for both boxes in order to be able to compare the volume occupied by the Qs in the two flows. Since the extraction of the Qs is computationally intensive, the number of instantaneous fields processed is limited to 27 for the ZPG TBL (box of 2.2×10^9 grid points) and 45 for the APG TBL (box of 1.7×10^8 grid points).

As in LFJ a so-called percolation threshold analysis has been performed to determine a value for H^* that gives an equilibrium between detecting only a few very big objects and detecting only a few small and very intense Qs. In contrast to LFJ however, the percolation test was performed for each Q type separately. The results shown in figure 10 are averages over 31 fields of the parameters in the APG TBL. Since the Qs are identified according to their uv quadrant, the ratio of the volume of the largest Q in one field, V_{lar}, to the volume of all identified Qs in that field, V_{tot}, does not tend to one as H^* decreases. Qs of quadrant i cannot fill the space since $(uv)_i = 0$ at points where the quadrant is not i. Moreover, Qs of a given quadrant remain disconnected when H^* is decreased since they are surrounded by Qs of other quadrants. Consequently, the ratio V_{lar}/V_{tot} seems to saturate as H^* is decreased, meaning that the size of the Qs no longer varies significantly. Nevertheless, a percolation crisis seems to take place in the approximate range $1.2 \leq H^* \leq 2.5$ for Q1, Q2 and Q4. A hyperbolic hole size of $H^* = 1.75$ is chosen because it is in the middle of this range and it maximizes the number of Q^-s. It is the same value as used by LFJ in turbulent channel flows.

The linear dimensions of the Qs are defined with a rectangular box circumscribing them, the sides of this box being denoted as Δx, Δy and Δz and the midheight position of the box y_c. Structures that are as long as the streamwise length of the extraction box, $\Delta x = B_x$, are disregarded because the length of these structures is undetermined. Similarly, very small Qs with a volume $V < (3\Delta x_g)^3$ are rejected because their sizes are not well resolved on the numerical grid.

With the present extraction procedure, a total of 184576 Qs are identified in the APG TBL and 441217 Qs in the ZPG TBL. The difference in number corresponds approximately to the difference in volume of the extraction boxes. As LFJ found in turbulent channel flows, Q^+s are less frequent than Q^-s in both TBLs, and they occupy a much smaller fraction of the space, less than 1% of the box volume against 4 to 5% for Q^-s. The difference in volume proportion is apparent from the perpective views of instantaneous Qs in Fig. 6. Q^- structures represent 57% and 52% of all Qs in the ZPG and APG TBL respectively. Table 3 summarizes

Table 2 Parameters of the Q extraction zones. B_x, B_y and B_z are the box dimensions along the three axes and δ_a is the average boundary layer thickness inside the box. N_f is the number of flow fields used

Flow	Re_θ	Re_m	Re_{zs}	H	$(B_x, B_y, B_z)/\delta_a$	N_f
ZPG TBL	4544-5801	10195-10811	6251-6599	1.38-1.37	4.51, 2.00, 10.57	27
APG TBL	2577-3916	9204-27889	5084-13413	1.97-3.42	4.99, 2.00, 4.09	45

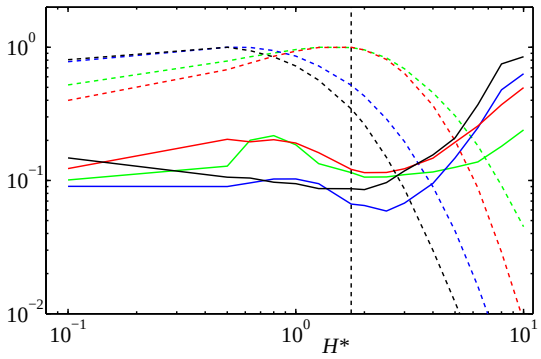

Fig. 10 Percolation diagram for the identification of Qs in the APG TBL: blue, Q1; red, Q2; black, Q3; green, Q4. Average over 31 fields of V_{lar}/V_{tot} (solid lines) and N/N_{max} (dashed lines). The vertical dashed line indicates the chosen hyperbolic hole size of $H^* = 1.75$

the number and volume proportions for the Q$^-$s. Although the number fraction of ejections and sweeps is higher in the ZPG TBL than in the large-defect TBL, the volume occupied by these structures is smaller (4.2% of the box volume against 5.3%). The reason lies in the different wall-normal distribution of these sweep and ejection motions in the two flows. In the ZPG TBL, 43% of all Q$^-$s are small near-wall structures (near-wall Qs are defined here as structures whose center is below 0.05δ) which is consistent with the fact that the mean shear is the strongest there [14]. In the large defect APG TBL, which has a very different mean shear distribution, only 10% of all ejections and sweeps are small near-wall structures.

Figure 11 shows the joint probability density function (pdf) of the minimum and maximum wall distances for the ejections and sweeps. The structures separate into two groups: structures reaching the wall region (wall-attached) and not reaching it (wall-detached). In both flows, the wall-attached Q$^-$s form the narrow vertical band of the joint pdf with $y_{min} < 0.05\delta$, while wall-detached structures form the wide diagonal band. Note that the name *wall-attached* can be misleading as it seems to imply that the structure remains attached to the wall during its whole life, which is usually not the case. In turbulent channel flows, Lozano et al. [14] have shown that wall-attached ejections are generally born with their base near the wall, but remain attached only for approximately 2/3 of their lives. Lozano et al. [14] found that attached sweeps are the mirror image of attached ejections with respect to the temporal evolutions of their size and wall-normal

Table 3 Number and volume proportions of the Q$^-$s (Q2s and Q4s)

Case	ZPG TBL	APG TBL
All Q$^-$s	57% of all Qs 4.2% of box volume	52% of all Qs 5.3% of box volume
Near-wall Q$^-$s ($y_c < 0.05\delta$)	43% of all Q$^-$s 2% of total volume of Q$^-$s	10% of all Q$^-$s 1% of total volume of Q$^-$s
Wall-attached Q$^-$s ($y_{min} < 0.05\delta$)	51% of all Q$^-$s 73% of total volume of Q$^-$s	35% of all Q$^-$s 58% of total volume of Q$^-$s

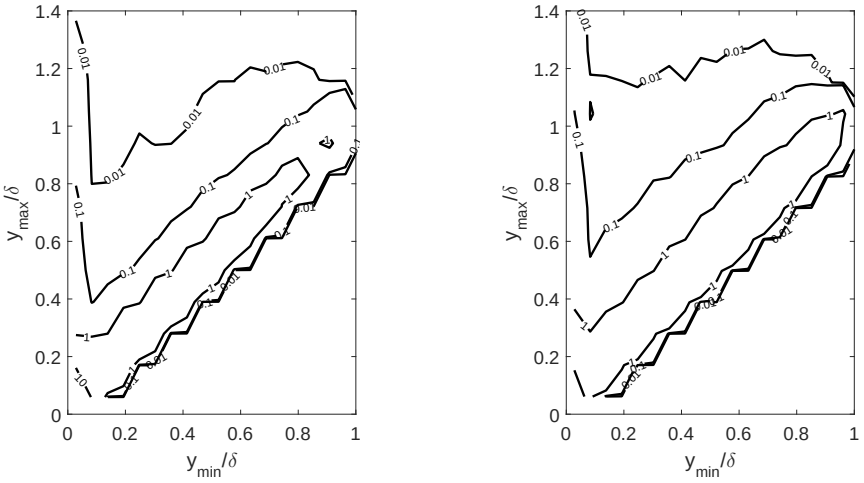

Fig. 11 Joint pdf of y_{min}/δ and y_{max}/δ for Q$^-$s. (a) ZPG TBL, (b) APG TBL. Contour levels are 0.01, 0.1, 1 and 10

position. They usually start as detached structures but become attached at about 1/3 of their lives and remain so thereafter.

It is seen from Fig. 11 that the height of Q$^-$s can exceed the boundary layer thickness. Wall-attached Q$^-$s almost as tall as 2δ are found in both flows. In the present APG flow the probabilities are higher everywhere, except near the origin. This implies that, as was discussed above, there are definitely less small Q$^-$s close to the wall, in proportion, in the APG TBL than in the ZPG TBL. For the detached Q$^-$s (diagonal band), the contours are wider in the vertical direction for the APG TBL, which indicates that the detached structures are generally taller in that flow. They are in fact bigger in all directions as it will be confirmed below.

Wall-attached Q2s and Q4s represent 35% of the total number of Q$^-$s and 58% of their volume (see Table 3). In the ZPG TBL, these percentages are respectively 51% and 73%. The number and size proportions of attached ejections and sweeps are therefore considerably reduced in a large-velocity-defect boundary layer. This is consistent with the fact that the turbulent activity is very small near the wall.

Figures 12 and 13 presents joint pdfs of the logarithms of the streamwise and wall-normal sizes, normalized with δ, of the boxes circumscribing Q2s and Q4s for attached and detached structures respectively. As in LFJ for turbulent channel flows, the Q2 and the Q4 structures have similar sizes, with Q2s slightly bigger for the biggest structures. The very small attached Q4s seen in the ZPG TBL (Fig. 12a) are streaky sweeps flattened against the wall [14]. They do not exist in the APG TBL.

The Q$^-$s in the APG TBL are generally bigger in all directions. But the largest structures are found in the ZPG TBL with attached Q2s that can reach the length of the extraction box $\Delta_x \approx 5\delta$ while being 3 times longer than they are tall and wide. For channel flows, LFJ found very long attached Q2s reaching $\Delta_x \approx 20h$ and $\Delta_y \approx \Delta_z \approx 2h$, where h is the channel half-height. The rapid streamwise variations and strong non-equilibrium state of the present APG TBL probably

prohibit the existence of such long motions. In this flow, the longest attached Q2s rarely exceed a length of 3δ.

In the ZPG TBL, the detached Q^-s (Fig. 13a) are globally smaller than their attached counterparts (Fig. 12a). LFJ observed that in turbulent channel flows, detached Q^-s and Q^+s are often background fluctuations of small size, of the order of a few Kolmogorov lengths, whose contributions to the Reynolds shear stress almost cancel. In the APG TBL, the situation is very different: the distribution of sizes of the detached Q^-s (Fig. 13b) is less different from that of the attached Q^-s (Fig. 12b).

In terms of aspect ratio, Fig. 12 shows that the attached structures tend to form a self-similar family of streamwise elongated structures, but much more so for the ZPG TBL with a linear law $\Delta_x \approx 3\Delta_y \approx 3\Delta_z$ identical to the law found by LFJ in channel flows. In the APG TBL, the law is $\Delta_x \approx 1.5\Delta_y \approx 1.5\Delta_z$. In both flows, the detached structures tend to be only slightly longer than they are tall and wide with $\Delta_x \approx 1.2\Delta_y \approx 1.2\Delta_z$.

5 Conclusions

The effects of strong adverse pressure gradients on the u and uv structures of turbulent boundary layers have been investigated through comparisons of the structures in a zero-pressure-gradient TBL and in a non-equilibrium large-defect TBL. The DNS database of the ZPG TBL is that of Sillero et al. [24]. The APG TBL comes from a new DNS intended to produce a flow with a large streamwise increase of the inner and outer pressure gradient parameters leading to separation at the end of the domain in the form of a very thin separation bubble. Both flows are at relatively high Reynolds numbers.

The present study focuses more on the structures found in the outer region since most of the turbulent activity is there in large-defect TBLs. Nevertheless, some information is also obtained on the near-wall structures. The findings are consistent with the fact that Reynolds stresses and production of turbulent energy diminish considerably in the near-wall region as the velocity defect increases. For instance, near-wall streaks tend to disappear in the large-defect zone of the flow and are replaced by more disorganized u motions. Near-wall Q2 and Q4 structures are also much less numerous in the large-defect TBL in comparison to the ZPG TBL. In the layer below $y = 0.05\delta$, they represent only 10% of all sweeps and ejections found throughout the boundary layer, while in the ZPG TBL they account for as much as 43% of the sweeps and ejections.

In the outer region of the large-defect TBL, the u structures tend to be shorter, less streaky, and more inclined with respect to the wall than in the ZPG TBL. Moreover, the two-point correlations suggest that near separation, the occurrence of side-by-side low- and high-speed structures is considerably reduced. The sweeps and ejections are generally bigger with respect to the boundary layer thickness in the large-defect boundary layer, even if the biggest structures are found in the ZPG TBL. The distinction between wall-attached and wall-detached structures is also not as pronounced. Contrary to the ZPG TBL, both types of structures have similar size distributions and occupy a similar space in the boundary layer. In the ZPG TBL, as in turbulent channel flows [13], the detached sweeps and ejections tend to be smaller than the attached ones.

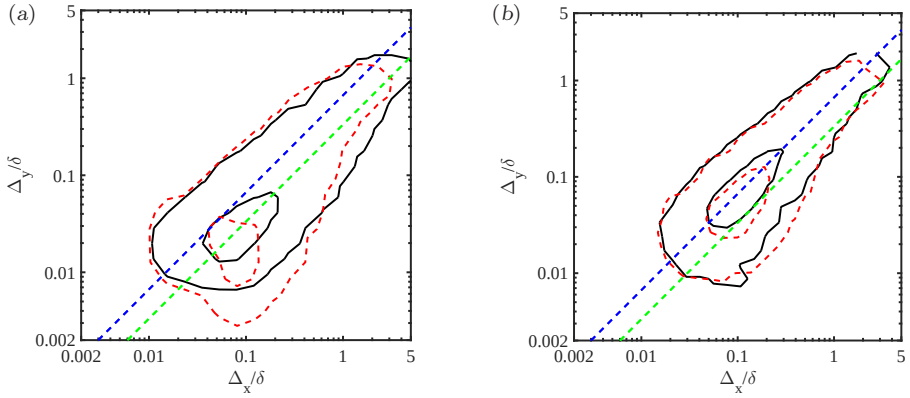

Fig. 12 Joint pdfs $p(\Delta_x/\delta, \Delta_y/\delta)$ of the logarithms of the sizes of the boxes circumscribing wall-attached Q2s (solid black) and Q4s (dashed red): (a) ZPG TBL, (b) APG TBL. The straight dashed lines are $\Delta_x = 1.5\Delta_y$ (blue) and $\Delta_x = 3.0\Delta_y$ (green)

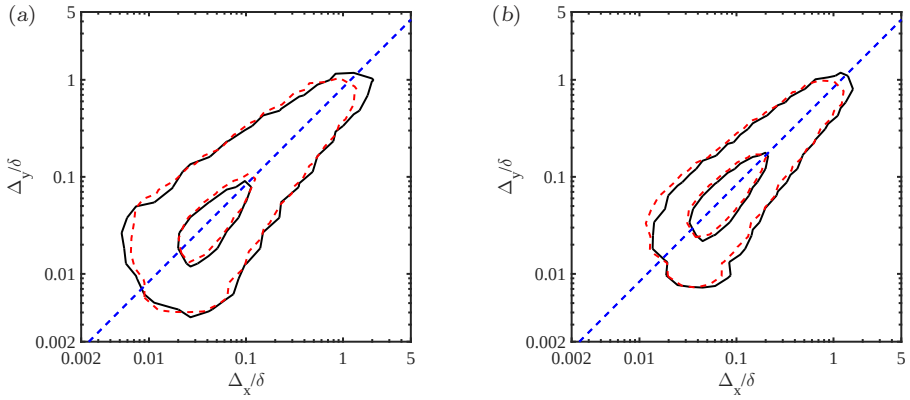

Fig. 13 Joint pdfs $p(\Delta_x/\delta, \Delta_y/\delta)$ of the logarithms of the sizes of the boxes circumscribing wall-detached Q2s (solid black) and Q4s (dashed red): (a) ZPG TBL, (b) APG TBL. The straight dashed blue lines are $\Delta_x = 1.2\Delta_y$

In both flows, the attached sweeps and ejections are more streamwise elongated than their detached counterparts but the difference in aspect ratio is much less for the APG TBL. The attached sweeps and ejections tend to form a family of self-similar structures with aspect ratios $\Delta_x \approx 3\Delta_y \approx 3\Delta_z$ in the ZPG TBL and $\Delta_x \approx 1.5\Delta_y \approx 1.5\Delta_z$ in the APG TBL. The streamwise elongation is therefore considerably reduced in a large-defect boundary layer. The detached structures also to tend form a self-similar family but with an identical aspect ratio in both flows, $\Delta_x \approx 1.2\Delta_y \approx 1.2\Delta_z$.

Acknowledgements Funded in part by the Multiflow program of the European Research Council. AGG and YM were supported in part respectively by ITU-BAP and NSERC of Canada. YM thanks TUBITAK (2221 Program) for supports during the collaboration stay

in Turkey. The computations were made possible by generous grants of computer time from Barcelona supercomputing center and from the national center for high performance computing of Turkey. The authors would like to thank Prof. Jiménez for organizing the First and Second Multiflow Summer Workshops, Juan Sillero and Prof. Jiménez for providing their ZPG TBL data and the programs for the two-point correlations, and Adrián Lozano-Durán and Prof. Jiménez for the processing programs for the Q structures analysis.

References

1. Adrian, R.J., Meinhart, C.D., Tomkins, C.D.: Vortex organization in the outer region of the turbulent boundary layer. Journal of Fluid Mechanics **422**, 1–54 (2000)
2. Chong, M.S., Soria, J., Perry, A.E., Chacin, J., Cantwell, B.J., Na, Y.: Turbulence structures of wall-bounded shear flows found using DNS data. Journal of Fluid Mechanics **357**, 225–247 (1998)
3. Elsberry K. Loeffler, F., Zhou, M., Wygnanski, I.: An experimental study of a boundary layer that is maintained on the verge of separation. J. Fluid Mech. **423**, 227–261 (2000)
4. Gungor, A.G., Maciel, Y., Simens, M.P., Soria, J.: Analysis of a turbulent boundary layer subjected to a strong adverse pressure gradient. Journal of Physics: Conference Series **506**, 012,007 (2014)
5. Gungor, A.G., Maciel, Y., Simens, M.P., Soria, J.: Scaling and statistics of large-defect adverse pressure gradient turbulent boundary layers. Intl J. Heat Fluid Flow **59**, 109–124 (2016)
6. Harun, Z., Monty, J.P., Mathis, R., Marusic, I.: Pressure gradient effects on the large-scale structure of turbulent boundary layers. Journal of Fluid Mechanics **715**, 477–498 (2013)
7. Hutchins, N., Marusic, I.: Evidence of very long meandering features in the logarithmic region of turbulent boundary layers. Journal of Fluid Mechanics **579** (2007)
8. Hwang, Y.: Statistical structure of self-sustaining attached eddies in turbulent channel flow. Journal of Fluid Mechanics **767**, 254–289 (2015)
9. Jiménez, J.: Near-wall turbulence. Physics of Fluids **25**(10) (2013)
10. Jiménez, J., Kawahara, G.: Dynamics of wall-bounded turbulence. In: P.A. Davidson, Y. Kaneda, K.R. Sreenivasan (eds.) Ten Chapters in Turbulence, pp. 221–268. Cambridge University Press (2013)
11. Krogstad, P.Å., Skåre, P.E.: Influence of a strong adverse pressure gradient on the turbulent structure in a boundary layer. Phys. Fluids **7**, 2014–2024 (1995)
12. Lee, J.H., Sung, H.J.: Structures in turbulent boundary layers subjected to adverse pressure gradients. J. Fluid Mech. **639**, 101–131 (2009)
13. Lozano-Durán, A., Flores, O., Jiménez, J.: The three-dimensional structure of momentum transfer in turbulent channels. J. Fluid Mech. **694**, 100–130 (2012)
14. Lozano-Durán, A., Jiménez, J.: Time-resolved evolution of coherent structures in turbulent channels: characterization of eddies and cascades. Journal of Fluid Mechanics **759**, 432–471 (2014)
15. Marquillie, M., Ehrenstein, U., Laval, J.P.: Instability of streaks in wall turbulence with adverse pressure gradient. Journal of Fluid Mechanics **681**, 205–240 (2011)
16. Marquillie, M., Laval, J.P., Dolganov, R.: Direct numerical simulation of a separated channel flow with a smooth profile. Journal of Turbulence (9) (2008)
17. Marusic, I., Adrian, R.: The eddies and scales of wall turbulence. In: P.A. Davidson, Y. Kaneda, K.R. Sreenivasan (eds.) Ten Chapters in Turbulence, pp. 176–220. Cambridge University Press (2013)
18. Na, Y., Moin, P.: Direct numerical simulation of separated turbulent boundary layer. J. Fluid Mech. **374**, 379–405 (1998)
19. Nagaosa, R., Handler, R.A.: Statistical analysis of coherent vortices near a free surface in a fully developed turbulence. Physics of Fluids **15**(2), 375–394 (2003)
20. Rahgozar, S., Maciel, Y.: Low-and high-speed structures in the outer region of an adverse-pressure-gradient turbulent boundary layer. Experimental Thermal and Fluid Science **35**(8), 15751587 (2011)
21. Rahgozar, S., Maciel, Y.: Statistical analysis of low- and high-speed large-scale structures in the outer region of an adverse pressure gradient turbulent boundary layer. Journal of Turbulence **13**, 1–24 (2012)

22. Robinson, S.K.: Coherent Motions in the Turbulent Boundary Layer. Annu. Rev. Fluid Mech. **23**(1), 601–639 (1991)
23. Shafiei Mayam, M.: Experimental study of the turbulence structures in a boundary layer subjected to a strong adverse pressure gradient. Ph.D. thesis, Laval University, Quebec City, Canada (2009)
24. Sillero, J., Jiménez, J., Moser, R.: One-point statistics for turbulent wall-bounded flows at Reynolds numbers up to $\delta^+ \approx 2000$. Physics of Fluids **25**, 105,102–1–16 (2013)
25. Sillero, J.A., Jimnez, J., Moser, R.D.: Two-point statistics for turbulent boundary layers and channels at Reynolds numbers up to $\delta^+ \approx 2000$. Physics of Fluids **26**(10), 105,109–1–30 (2014)
26. Simens, M., Jiménez, J., Hoyas, S., Mizuno, Y.: A high-resolution code for turbulent boundary layers. Journal of Computational Physics **228**, 4218–4231 (2009)
27. Skåre, P.E., Krogstad, P.Å.: A turbulent equilibrium boundary layer near separation. J. Fluid Mech. **272**, 319–348 (1994)
28. Townsend, A.: The structure of turbulent shear flow. Cambridge University Press (1956)
29. Wark, C.E., Nagib, H.M.: Experimental investigation of coherent structures in turbulent boundary layers. J. Fluid Mech. **230**, 183–208 (1991)